Lithium nitridonickelate as anode coupled with argyrodite electrolyte for all-solid-state lithium-ion batteries

Yaxin Qu, Mickael Mateos, Nicolas Emery, Fermin Cuevas, Dimitri Mercier, Sandrine Zanna, Rios de Anda Agustin, Narimane Meziani, Junxian Zhang

Lithium nitridonickelate as anode coupled with argyrodite electrolyte for all-solid-state lithium-ion batteries

Yaxin Qu[1], Mickael Mateos[1,*], Nicolas Emery[1], Fermin Cuevas[1], Dimitri Mercier[2], Sandrine Zanna[2], Agustin Rios de Anda[1], Narimane Meziani[1], Junxian Zhang[1]

(1) Univ Paris-Est Creteil, CNRS, ICMPE (UMR 7182), 2 rue Henri Dunant, F-94320 Thiais, France

(2) PSL Research University, CNRS – Chimie ParisTech, Institut de Recherche de Chimie Paris, Physical Chemistry of Surfaces Group, 11 Rue Pierre et Marie Curie, 75005 Paris, France

Abstract

Argyrodites Li_6PS_5X (X = Cl, Br) have attracted growing interest due to their exceptional ionic conductivity and ductility, making them promising electrolytes for all-solid-state lithium-ion batteries. However, their poor electrochemical stability at very low potential limits the use of lithium metal as a negative electrode. Instead of using Li-In alloy, this study explores the electrochemical properties of lithium nitridonickelate $Li_{2.07}Ni_{0.62}N$ as an alternative negative electrode material, paired with balled milled argyrodite Li_6PS_5Br. The same electrochemical storage mechanism observed in liquid media is at work here, exhibiting a solid-solution profile along with low lattice expansion through the reversible insertion mechanism. By adjusting the potential window to minimize argyrodite degradation, the active material delivered a stable capacity of 125 mAh g^{-1} over 60 cycles at C/25, with a mean working potential of 0.5 V at room temperature. The excellent capacity retention was achieved up to C/10, demonstrating good compatibility between the argyrodite solid electrolyte and lithium nitridonickelate negative electrode.

Keywords: argyrodite, insertion mechanism, solid electrolyte, Li-ion Batteries, mechanical-milling.

Highlights:

- $Li_{2.07}Ni_{0.62}N$ exhibits a reversible capacity of 125 mAh g^{-1} at C/25 over 60 cycles.
- The same insertion mechanism is observed in the solid-state configuration.
- Overpotentials and lattice volume expansion are minimized during cycling.
- Adjusting the lower cott-off potential during lithiation can extend cycling life.

Introduction

Although solid-state batteries were introduced and developed prior to conventional lithium-ion batteries (LIBs), the rapid commercialization of low-cost and easily manufactured LIBs with carbonate liquid electrolytes hindered the advancement of solid-state batteries [1]. However, recently, the increasing demand for batteries capable of providing higher energy and current densities (up to 500-600 Wh kg^{-1} and 2-3 kW kg^{-1}) [2] along with enhanced safety unattainable by traditional LIBs has led to a resurgence of interest in solid-state batteries technology [3,4].

In the realm of All-Solid-State Lithium Batteries (ASSLIBs), the use of a solid electrolyte instead of a liquid electrolyte eliminates the need for a separator and consequently reduces issues related to flammability and short circuits. This enhances safety and stability while potentially improving energy density and cycle life [5–7].

Sulfide-based solid-state electrolytes (SSEs) demonstrate excellent ionic conductivity and possess a much smaller Young's modulus compared to their oxide counterparts. This characteristic facilitates more intimate particle contact in electrode composites, particularly at the interface between the active material and the electrolyte [8,9]. Such efficient contact makes sulfide-based SSEs particularly advantageous for integration into ASSLIBs [10,11]. Significant advancements occurred in the 2010s with the discovery of sulfide-based SSEs exhibiting ionic conductivities surpassing those of traditional liquid electrolytes [12]. Notably, the LGPS family, including $Li_{10}GeP_2S_{12}$ and its substituted counterpart $Li_{6.6}P_{0.4}Ge_{0.6}S_5I$, was found to have conductivities of 12 mS cm^{-1} and 18 mS cm^{-1} at room temperature (RT), respectively [12].

The argyrodite family, $Li_{7-y}PS_{6-y}X_y$ (X = Cl, Br), with its face-centered cubic structure, is also an excellent lithium-ion conductor due to the partial substitution of sulfide ions by halogen ions (Cl^-, Br^-). This substitution has various beneficial effects, such as the creation of cation vacancies and increased polarizability, which facilitate lithium diffusion within the structure [10]. However, argyrodite faces several challenges, particularly due to its narrow electrochemical window, which lies between 0.8 V and 1.7 V [13,14]. At low potentials, the decomposition of argyrodite through the reduction of phosphorus atoms generates secondary products such as Li_2S, Li_3P, P, and LiX, which significantly influence the pathways of lithium ions at the electrode-electrolyte interface [13,15]. Furthermore, the growth of dendrites from the lithium metal anode cannot be completely avoided, leading to critical current densities ranging from 0.1 to 1 mA cm^{-2} [16–20].

In ASSLIB based on a sulfide electrolyte, the graphite anode demonstrates robust long-term performance at low current densities (60 μA cm^{-2}), achieving a capacity of almost 300 mAh g^{-1} during 400 cycles [21]. However, certain limitations arise, particularly the formation of degradation products such as Li_2S and Li_xP at the electrolyte-graphite interface, resulting from the low working potentials (0.1 V). Furthermore, rapid cycling negatively impacts the electrochemical performances, primarily due to the development of cracks within the composite electrode and insufficient percolation of ion-conducting particles [21].

The Li-In alloy anode, which operates at a potential of 0.6 V vs. $Li/Li^{+,}$ effectively mitigates dendrite formation and prevents the decomposition of argyrodite at the electrode-

electrolyte interface, thus enabling stable long-term plating/stripping cycles and high-rate cycling [17,22]. Nevertheless, the high cost of indium limits its application in ASSLIBs on an industrial scale. As a result, alternative, lower-cost alloys, such as those based on tin (Sn) and silicon (Si), have attracted increasing interest for use in ASSLIBs [23,24]. Sn-based anodes, with a working potential of 0.4 V vs. Li^+/Li, offer high capacities when combined with sulfide electrolytes (600 mAh g^{-1}). However, materials that rely on alloying or conversion reactions face significant challenges due to the difficulty in maintaining interface stability, primarily resulting from substantial volume changes [24].

A promising approach is to develop anode materials based on insertion mechanisms, characterized by low volume expansion and a working potential similar to that of the Li-In alloy, to mitigate argyrodite degradation and support long-term cycling stability. Lithium titanate oxide $Li_4Ti_5O_{12}$, meets many of these requirements, offering a working potential of 1.5 V vs. Li^+/Li and a capacity of 160 mAh g^{-1} in argyrodite-based ASSLIBs [25]. However, its high working potential limits the energy density and low ionic conductivity (10^{-13} to 10^{-9} S cm^{-1}) remains a significant challenge [26,27].

Following a similar approach, lithium transition metal nitrides offer an intriguing alternative, featuring two distinct structural types: anti-fluorite 3D structures, such as Li_7MnN_4 [28,29], and Li_3N-type layered structures with the general formula $Li_{3-xy}M_xN$ (M = Co, Ni, Cu; y = oxidation state of metal) [30–33]. Among these layered transition metal nitrides, the the $Li_{3-1.5x}Ni_xN$ solid solution, particularly $Li_2Ni_{0.67}N$, has recently emerged as a promising negative electrode material for LiBs. Within a potential range of 0.02-1.25 V vs. Li+/Li, this material has demonstrated a stable specific capacity of up to 200 mAh g^{-1} over 100 cycles [35,36]. Its structural behavior exhibits near-complete reversibility with minimal volume change (2%), indicating near zero-strain behavior. While Li_3N has been utilized as a protective anode layer in ASSLIBs [34], the use of $Li_{3-xy}M_xN$ layered structures as anode materials in ASSLIBs remains unexplored to our knowledge.

The present work aims to investigate the nitride compound $Li_{2.07}Ni_{0.62}N$ as a negative electrode material in all-solid-state batteries, in conjunction with ball-milled bromide argyrodite. The study comprehensively explores the intrinsic properties of the electrolyte, including its crystallographic structure and morphology, ionic conductivity, and stability against lithium metal. Subsequently, the research focuses on the electrochemical study of the coupling with nitride, comparing it with a liquid electrolyte medium to gain insights into both the energy storage and degradation mechanisms.

2. Experimental

2.1 Synthesis

Reagent-grade Li_2S (Sigma Aldrich 99%), P_2S_5 (Sigma Aldrich 99%), and LiBr (Sigma Aldrich 99%), powders were used as received and mixed in stoichiometric proportions according to the target composition Li_6PS_5Br. A total of 2 g of precursors was sealed in a tungsten carbide (WC) jar (45 ml) with 10 WC balls (ø = 10 mm). Mechanical milling was

performed using planetary milling (Fritch Pulverisette 7) at a speed of 600 rpm and a total milling time of 10 h with a 15-minute resting step per milling hour. All the experimental processes were performed in a glove box under dry Ar (O_2 < 4 ppm, H_2O < 1 ppm).

Lithium nitridonickelate was prepared by solid-state reaction under a nitrogen atmosphere. A mixture of Li_3N (Alpha Aesar, 99.4 % metal basis) and metallic Ni powders was thoroughly ground in an agate mortar and pressed into pellets (13mm diameter, ~6-8 mm thick). In an alumina crucible, the pellet was then transferred into a stainless-steel reactor, and thermal treatment at 720°C for 12 h under N_2 flux was performed. The sample was surrounded by 2 crucibles filled with a titanium sponge to trap possible oxygen traces in the nitrogen gas. The Ni/Li_3N molar ratio was fixed at 0.95, which led under these conditions to $Li_{2.07}Ni_{0.62}N$ [35].

2.2 Structural characterization

Laboratory X-ray powder diffraction (XRPD) patterns of argyrodites were collected over a 2θ range of 10 – 90° with a step of 0.04° and an integration time of 32 s / step on a D8 advance diffractometer with Cu Kα radiation (λ = 1.54178 Å), flat plate, Bragg Brentano geometry, and backscattered rear graphite monochromator. XRPD patterns of lithium nitridonickelate were collected using a Panalytical X'pert Pro diffractometer using Co Kα radiation (λ = 1.7889 Å) and a PIXCEL 1D linear detector. To prevent any degradation of both materials with moisture or oxygen, powders were placed in an airtight polymer sample holder under argon. Structures were refined by the Rietveld method using either Fullprof suite software [36] or BRUKER Topas V7. Since two different wavelengths were used to characterize our materials, all the diffraction patterns within this article are plotted as a function of the scattering vector Q and not the scattering angle (θ) to facilitate comparison. The relation between these two parameters is $Q(Å^{-1}) = 4\pi\sin(\theta)/\lambda$. The recorded patterns in 2θ are provided in the supplementary information (SI).

2.3 Surface characterizations

X-ray photoelectron spectroscopy (XPS) analysis was performed using a ThermoElectron ESCALAB 250 Xi spectrometer with monochromatized Al Kα radiation (1486.6 eV) operating at a pressure of approximately 10^{-10} mbar. The spectrometer was coupled to a glovebox to prevent any sample air exposure prior to analysis. The analyzer pass energy was set to 100 eV for survey spectra and 20 eV for high-resolution spectra. Curve fitting of the spectra was conducted using Thermo Electron's "Avantage" software, with all spectra calibrated versus the binding energy (BE) of hydrocarbons (C-H and C-C) at 285.0 eV. All deconvolutions were performed with a full width at half maximum (FWHM) variation of ± 0.2 eV.

The morphology of argyrodite and nitride were examined by Scanning Electron Microscopy (SEM) using a SEM-FEG MERLIN from Zeiss (Jena, Germany), operated in secondary electron mode with a 15 keV incident beam

2.4 Electrochemical characterizations

To assess the ionic conductivity of the argyrodite, the powders were pelletized by uniaxial pressing at 2 tons using a 6 mm diameter die. The resulting ~1 mm thick pellet was placed between two carbon papers (Papyex®) and enclosed within a coin cell CR2032, which was then introduced into a conductivity cell (CESH-e, Biologic). Impedance measurements were obtained using a multichannel potentiostat (VMP3, Biologic) over a frequency range of 400 kHz to 100 Hz with an amplitude of 30 mV. The temperature range was controlled between 20 and 80°C using a Peltier system (ITS-e, Biologic).

The stability of the interface between lithium metal and bromide argyrodite was tested using galvanostatic cycling in a symmetrical cell, consisting of a bromide argyrodite pellet sandwiched between two lithium foils (0.25 mm thickness, 99.8%, Chempure). Galvanostatic cycling was initiated with a fixed time step of 30 minutes, applying increasing current densities of 20, 40, 100, and 200 μA cm^{-2}. Subsequently, a 10-hour time step was employed with a constant current density of 40 μA cm^{-2} to assess long-term stability.

Cyclic voltammetry was conducted to evaluate the potential stability range of the argyrodite. The experimental setup consisted of a three-layer pellet configuration with two electrodes. The first layer contained a composite of argyrodite (75 wt.%) and vapor-grown carbon fiber (CVGF, 25 wt.%, Showa Denko KK, Japan). The second layer works as the solid electrolyte in the middle, and the third layer serves as the reference and counter electrode using Li metal foil. Cyclic voltammetry scans were performed at a scan rate of 10 μV s^{-1} from 0.02 to 1 V vs. Li^+/Li starting with a cathodic sweep.

All solid-state half-cells were assembled using the cold press method, with a diameter of 6 mm and a typical thickness of 1 mm. These cells were composed of a composite of active material lithium nitridonickelate $Li_{2.07}Ni_{0.62}N$ (45 wt.%), CVGF (5 wt.%), and argyrodite (50 wt.%) as the working electrode, with an active mass loading of 5 mg cm^{-2}, argyrodite as electrolyte with a typical mass of 40 mg and a lithium disk as the counter electrode.

As reported, the experimental specific capacity of $Li_2Ni_{0.67}N$ does not exceed 210 mAh g^{-1} at 20 mA g^{-1}, which corresponds to 78% of the theoretical value of 267 mAh g^{-1} (0.67 Li exchanged) [37,38]. Accordingly, for the current composition of $Li_{2.07}Ni_{0.62}N$, the theoretical value is expected to be 255 mAh g^{-1} (0.62 Li exchanged) and the maximum experimental capacity is anticipated at 200 mAh g^{-1}. Therefore, a 1C rate corresponds to 200 mA g^{-1}. All potentials will be referenced to Li^+/Li couple and all gravimetric variables will be calculated using the mass of active material. All these measurements were performed at room temperature.

2.5 Operando XRD analysis

A Leriche-type cell (modified Swagelok) [39] was used in reflection mode to collect operando X-ray diffraction (XRD) data of half-cell batteries constructed with a solid-state electrolyte. Pellets with a diameter of 10 mm and a thickness of approximately 1 mm were arranged such that the active nitride material was in direct contact with the top beryllium window, while the lithium disk counter electrode was placed in contact with a rear stainless-steel spacer. A spring ensured good contact and maintained the conductivity of the assembly.

The Panalytical diffractometer with Co-Kα radiation was employed to collect diffraction patterns in the angular range of 20-80° with a step size of 0.013°, over an acquisition time of 30 minutes during galvanostatic cycling at 5.8 mA g^{-1} in the 0.12 – 1 V vs. Li^+/Li voltage window.

3. Results and discussion

3.1 Characterization of ball-milled argyrodite

The XRPD pattern of the ball-milled compound and its Rietveld analysis are shown in Figure 1b (Figure S1 for the X-axis in 2θ), and the obtained crystallographic data are summarized in Table 1. The diffraction peaks correspond to the argyrodite Li_6PS_5Br cubic structure (SG $F\bar{4}3m$) with a lattice parameter of 9.962(1) Å, and no secondary phases were detected. This lattice parameter is consistent with reported values [40–42]. The crystallite size obtained by Rietveld analysis is 11 nm. SEM micrographs reveal poor crystallinity, characterized by irregular particles and agglomerates ranging in size from a few hundred nanometers to ten micrometers (Figure S2).

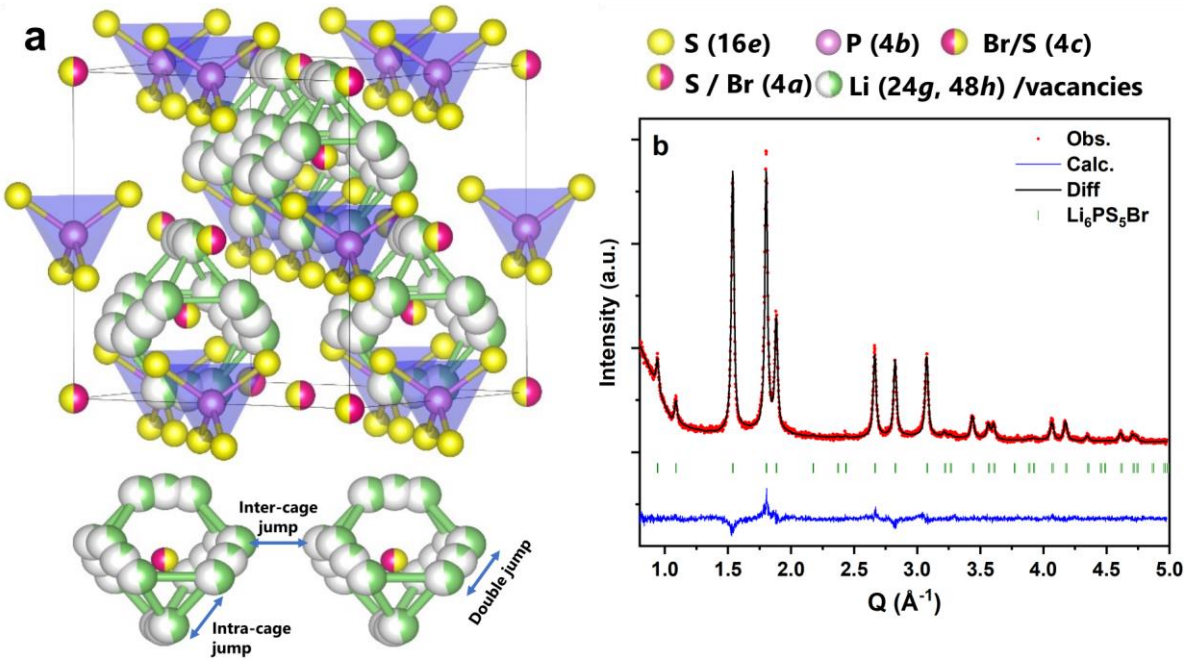

Figure 1 (a) Structural representation of the Li_6PS_5Br. (b) XRPD pattern and corresponding Rietveld refinement of the ball-milled Li_6PS_5Br sample.

Table 1. Crystallographic data obtained from Rietveld analysis of ball-milled Li_6PS_5Br. Only the parameters in *italics* have been refined as compared to the crystal structure reported [43,44]. Standard deviations for the last digit are given in parentheses.

Space group $F\bar{4}3m$, a = 9.962(1) Å
Fit residuals: R_{wp} = 7.21%, R_B = 3.55%, χ^2 = 1.51

Atom	site	*x*	*y*	*z*	Occupancy (%)
Br	**4*a***	0.000	0.000	0.000	*52(1)*
S	**4*a***	0.000	0.000	0.000	*48(1)*
P	**4*b***	0.500	0.500	0.500	100
S	**4*c***	0.250	0.250	0.250	*52(1)*
Br	**4*c***	0.250	0.250	0.250	*48(1)*
S	**16*e***	*0.621(1)*	*0.621(1)*	*0.621(1)*	100
Li	**48*h***	0.193	0.193	0.025	46
Li	**24*g***	0.017	0.250	0.250	8

As previously reported [45,46], due to their similar ionic radii, S^{2-} and Br^- ions are mixed between the 4*a* and 4*c* sites, resulting in an anionic disorder (see Figure 1a). The Rietveld analysis confirms the presence of anionic disorder between S^{2-} and Br^- ions, with the ratio of Br^-/S^{2-} close to 50% in the 4*a* and 4*c* sites. Such disorder in Li_6PS_5X (*X* = I, Br, Cl) argyrodites strongly affects their lithium transport properties [47–51]. In the anion-ordered Li_6PS_5X structure, the X^- anions occupy the 4*a* sites, forming a cubic-close-packed lattice (see Figure 1a). The PS_4^{3-} units occupy the octahedral sites, with P and S on the Wyckoff 4*b* and 16*e* positions, respectively. The S^{2-} anions occupy the 4*c* sites (half of the tetrahedral sites), which are surrounded by a polyhedral cage partially occupied by Li^+ cations at the 48*h* and 24*g* sites. Li_6PS_5I adopts an ordered structure due to the large ionic radius of iodide, resulting in poor ionic conductivity (10^{-3} mS cm^{-1}) [47,52]. In contrast, Li_6PS_5Cl and Li_6PS_5Br display anti-site disorder with higher ionic conductivity ranging from 1 to 10 mS cm^{-1} [45,46]. High-resolution neutron diffraction analysis has shown that this anion disorder leads to local charge inhomogeneity and creates new intermediate Li^+ sites that favor Li ion diffusion [50].

3.2 Ionic conductivity

The impedance response of the $LiPS_5Br$ pellet is displayed as a Nyquist plot in Figure 2a. Based on the shape of the curve, an R-Q series circuit model was used for fitting, where R represents the resistive properties and Q represents the dielectric properties of the material, modeled as a Constant Phase Element (CPE), equivalent to an imperfect capacitor.

An ionic conductivity of 0.75(4) mS cm^{-1} at room temperature (RT, 25°C) was obtained. The shift towards lower impedance in the Nyquist plots with increasing temperature indicates that Li^+ conduction is thermally activated. An Arrhenius plot of the ionic conductivity shown in Figure 2b displays an activation energy of 0.32(1) eV. Temperature dependence of the diffusion-induced ^{7}Li NMR spin-lattice relaxation rates provides an activation energy close to the previous one (Figure S3). DC polarization measurements demonstrate the negligible electronic conductivity of 5.10^{-9} S cm^{-1} for the balled-milled Li_6PS_5Br electrolyte (see Figure S4).

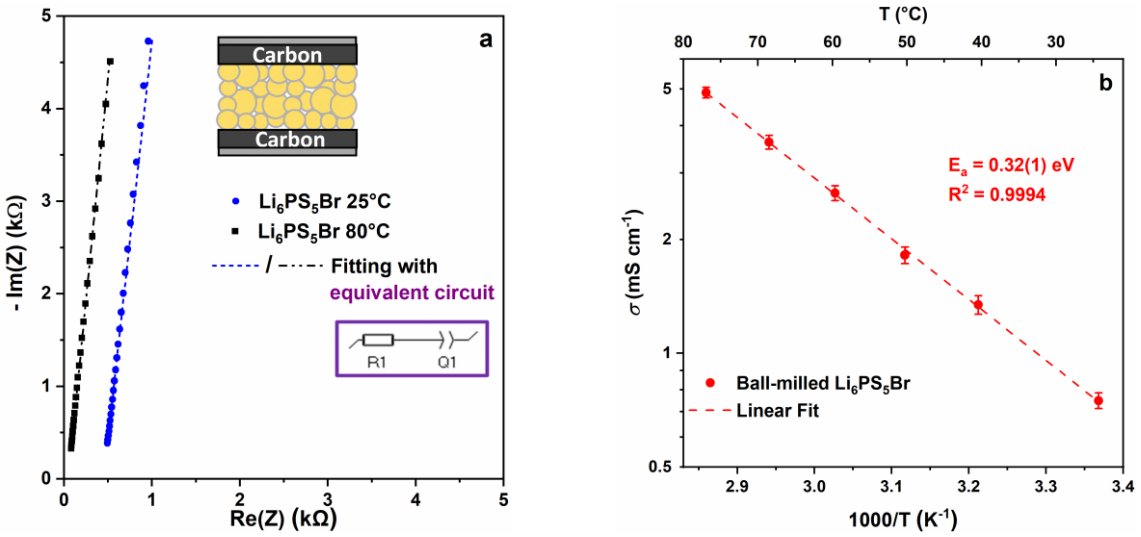

Figure 2: (a) Nyquist plot of ball-milled Li_6PS_5Br at room temperature (in blue) and 80°C (in black). (b) Arrhenius plots in the temperature range from 25 to 80 °C.

Ball milling is an effective synthesis method for argyrodite. Historically, milling times have been quite long (15–24 hours) with high ball-to-powder ratios and high rotating speeds. Various materials for the balls and jars, such as agate, zirconia, and tungsten carbide (WC), have been used, but a ball-to-powder ratio greater than 30 is typically required for successful synthesis [42,53,54]. In our work, by using WC jars and balls, we obtained single-phase samples after 10 hours of milling at 600 rpm, achieving an ionic conductivity of 0.75 mS cm^{-1} which is high enough for use as a solid electrolyte. Similar ionic conductivities were obtained on balled-milled argyrodite with an ionic conductivity of 0.8 mS cm^{-1} [55] and reported conductivities for annealed Li_6PS_5Br samples to lie between 0.7 and 2 mS cm^{-1} [53,56,57], depending on the synthesize conditions, the pelletization method, the setup for conductivity measurements and so on. Higher conductivities can be obtained with higher bromide content $Li_{5.5}PS_{4.5}Br_{1.5}$, reaching 4 to 8 mS cm^{-1} [55,56].

3.3 Interface stability of bromide argyrodite versus Li metal

Besides the determination of the electrochemical stability window (see Figure S5), the interfacial stability of the bromide argyrodite in contact with lithium metal has been investigated using galvanostatic cycling of a Li metal | Li_6PS_5Br | Li metal symmetric cell. The lithium ions are plated and stripped on and from the surface of the lithium metal electrode, respectively, and go through the argyrodite pellet which should act as an ionic conductor. Figure 3a shows an increasing polarization of the cell upon increasing current density. The ohmic law was observed for current densities ranging from 40 to 200 µA cm^{-2}, with a resulting total resistance of 550 ± 30 Ω which is slightly higher than the bulk resistance estimated to be 410 Ω from the ionic conductivity previously determined. This increase can be attributed to the formation of a degradation layer in contact with lithium metal which introduces additional resistance [58,59]. The resulting resistance at a current density of 20 µA cm^{-2} was higher, at

670 Ω, probably because the contact between Li metal and argyrodite was not yet well established. At 250 µA cm^{-2}, a sudden drop in potential from 40 to 4 mV was observed, indicating the formation of dendrites within the argyrodite, leading to the short-circuit of the solid electrolyte pellet. This well-known phenomenon arises from the formation of voids at the interface during lithium stripping. This creates spike effects which lead to the localized growth of lithium dendrites passing through the porosity of the solid electrolyte [22].

The present critical current density is consistent with the previous result for Li_6PS_5X (X= Cl, Br) where the current lies between 0.1 and 1 mA cm^{-2}, depending on the protocol (time, number of cycles, method of pelletization…) [54,55,60,61]. This critical current density represents a limiting factor that prevents the application of high C-rate for subsequent half-cell $Li|Li_6PS_5Br|Li_{2.07}Ni_{0.62}N$ cycling. The long-term stability of the symmetric cell was investigated with a longer time step (10h) and current density of 40 µA cm^{-2} in Figure 3b which corresponds to the long-term cycling at 8 mA g^{-1} of the half-cell (Figure 5). The polarization remains roughly stable during 1000 hours at 6.2 ± 0.7 mV.

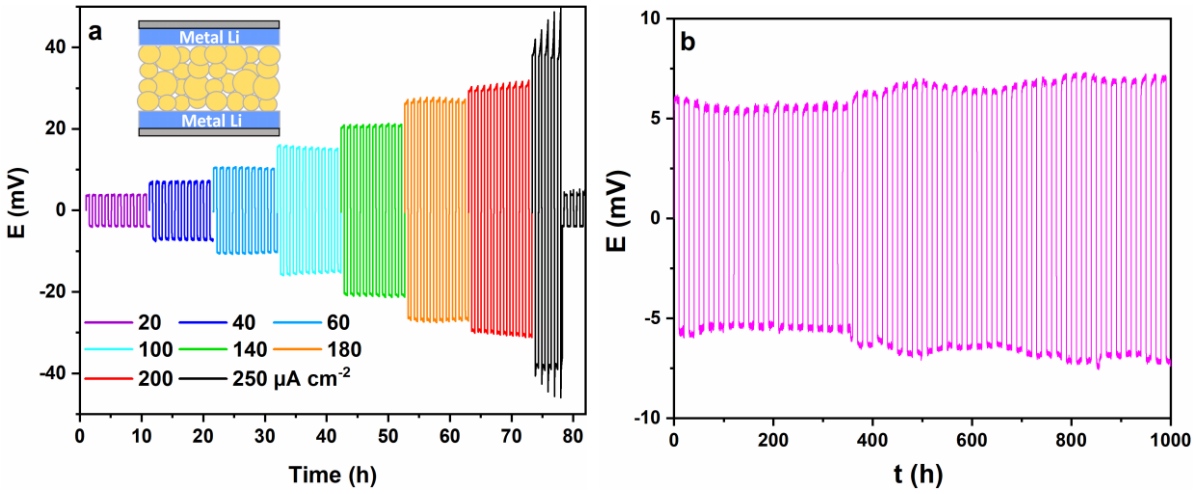

Figure 3: Polarization of the $Li/Li_6PS_5Br/Li$ symmetrical cell (a) under an increasing current density of 20, 40, 60, 100, 140, 180, 200, and 250 µA cm^{-2} with 30 min current step-up, 10 cycles per every current density (b) under a constant current density of 40 µA cm^{-2} with 10 h current step-up.

3.4 Structural characterization of the lithiated nitridonickelate

The XRPD pattern of the lithiated nitrodonickelate, along with its Rietveld analysis, is presented in Figure 4a (Figure S6 shows the X-axis in 2θ). The diffraction pattern fits well with the *P6/mmm* Li_3N-structure, where nickel and lithium cations share the interlayer 1*b* site, the nitrogen anion the 1*a* site, and the 2*c* site is partially occupied by lithium ions. The obtained cell parameters are $a = 3.753(1)$ Å and $c = 3.554(1)$ Å. Due to the nitride's composition predominantly consisting of light elements (N and Li), precise determination of the composition

via Rietveld analysis is challenging. According to the literature [35], nickel ions in these nitrides exhibit an intermediate valence state of $Ni^{1.5+}$, and the cell parameters vary linearly with the nickel content. Consequently, the determined cell parameters suggest a composition of $Li_{2.07}Ni_{0.62}N$, which is in good agreement with the initial Ni/Li_3N molar ratio of 0.95. The SEM images of the pristine nitride powder in Figure 4b show that it is composed of irregular platelet-shaped particles of micrometric size, forming agglomerates up to 100 µm in size.

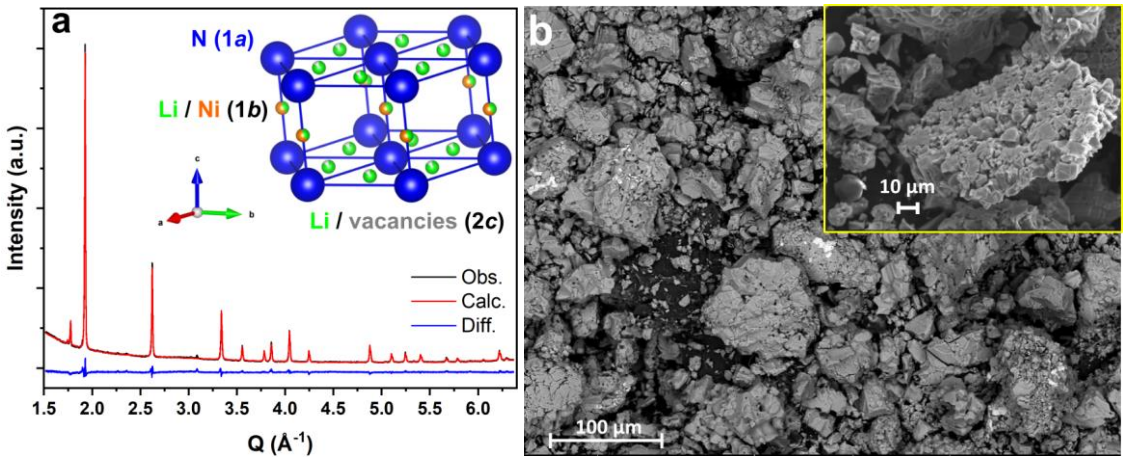

Figure 4: (a) Rietveld refinement of the $Li_{2.07}Ni_{0.62}N$ XRPD pattern and its structural representation with nitrogen in blue, nickel in orange, lithium in green, and vacancies in gray (b) SEM image of $Li_{2.07}Ni_{0.62}N$.

3.5 Electrochemical properties of $Li_{2.07}Ni_{0.62}N$ in liquid medium

To establish a reference for the electrochemical properties of $Li_{2.07}Ni_{0.62}N$, galvanostatic cycling was performed in a liquid medium. The preparation of the liquid half-cell followed recent literature guidelines [37,38]. The reactions occurring in the batteries can be described as follows: *i*) the starting material undergoes oxidation of $Ni^{1.5+}$ to Ni^{2+}, extracting 0.31 Li^+ ions from the 2*c* sites to form the delithiated phase $Li_{1.76}Ni_{0.62}N$ (Eq. 1), and *ii*) the reversible charge (lithiation) – discharge (delithiation) reaction, with a maximum *x* value of 0.62, corresponding to the number of vacancies available in the 2*c* sites for the delithiated phase.

$$Li_{2.07}\square_{0.31}Ni_{0.62}N \longrightarrow Li_{1.76}\square_{0.62}Ni_{0.62}N + 0.31e^- + 0.31Li^+ \quad \text{(Eq. 1)}$$

$$Li_{1.76}\square_{0.62}Ni_{0.62}N + \mathrm{x}\, e^- + \mathrm{x}\, Li^+ \leftrightharpoons Li_{1.76+x}\square_{0.62-x}Ni_{0.62}N \quad \text{(Eq. 2)}$$

The amount of 0.62 Li^+ exchanged per unit formula corresponds to a specific capacity of 255 mAh g^{-1}. However, the expected experimental capacity should be around 200 mAh g^{-1} at 20 mA g^{-1}. As reported, the theoretical specific capacity of $Li_2Ni_{0.67}N$ reaches 267 mAh g^{-1} while the experimental specific capacity does not exceed 210 mAh g^{-1} at 20 mA g^{-1} [37]. It has been demonstrated that it is not possible to reduce nickel ions down to Ni^+ which implies remaining vacancies in the 2*c* sites of the lithiated form.

Figure 5 illustrates the charge/discharge galvanostatic voltage curves at 40 mA g^{-1} within a voltage range of 0.02 to 1.25 V vs. Li^+/Li for the assembled $Li_{2.07}Ni_{0.62}N$ in a liquid medium. The upper voltage cutoff has been chosen to avoid the higher potential that induced the degradation of the nitride. The degradation of lithium-transition metal nitride is characterized by a flat plateau at a potential depending on the amount and the nature of the transition metal [31]. The initial delithiation sweep begins at a potential of 0.38 V, with the extraction of 0.25 Li^+. It is consistent with the oxidation of $Ni^{+1.5}$ to a valence close to +2, which confirms the intermediate valence reported [37]. Then, the first cycle exhibited a capacity upon lithiation and delithiation of 192 and 166 mAh g^{-1}, respectively resulting in a coulombic efficiency of 86%. This irreversible reaction, attributed to the formation of the solid-electrolyte interphase (SEI) [37,38] tends to shift the potential curve along the x-axis, leading to an apparent higher hysteresis during the initial cycles. The reversible capacity and potential profile observed for the $Li_{2.07}Ni_{0.62}N$ compound aligns well with the solid-solution mechanism previously reported for lithiated nitrodonickelate [33,63,64].

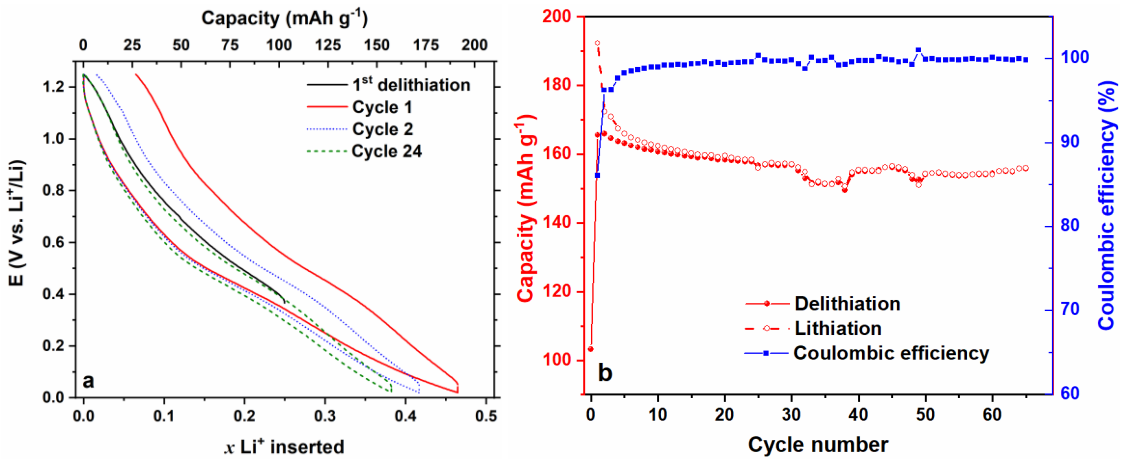

Figure 5: (a) Galvanostatic voltage profile for the assembled $Li_{2.07}Ni_{0.62}N$ in liquid medium at 40 mA g^{-1} (C/5) in the 0.02 – 1.25 V range. (b) Evolution of the capacities and coulombic efficiency upon cycling.

3.6 Electrochemical properties of $Li_{2.07}Ni_{0.62}N/Li_6PS_5Br/Li$ all-solid-state batteries

The morphology and the chemical distribution of the anode composite were examined by SEM. The Energy Dispersive X-ray (EDX) chemical mapping of the $Li_{2.07}Ni_{0.62}N$ (45 wt.%) / CVGF (5 wt.%) / Li_6PS_5Br (50 wt.%) composite revealed a relatively homogeneous mixture where argyrodite (identified by the concomitance of Br, S, and P regions) surrounds the nitride particles (concomitance of N, and Ni regions) and forms a percolating network that facilitates lithium diffusion (Figure S7a-e). Backscattered electron images (Figure S7f) clearly show the presence of fibers from the CVGF.

In ASSLB, a C-rate of C/25 was used for galvanostatic cycling with a potential window restrained between 0.02 and 1V to avoid the degradation of nitride which starts at around 1.2 V at this low rate. The OCV voltage is around 0.44 V, which is consistent with the value observed in liquid media (0.38 V). With an upper cutoff voltage of 1 V, the first delithiation leads to the extraction of 0.17 Li^+ with a solid solution behavior, as expected. Thus, it suggests an absence of chemical degradation between the nitride and the argyrodite.

The galvanostatic profile remains stable between cycle 1 and cycle 16 with a reversible gravimetric capacity of around 150 mAh g^{-1}, corresponding to 0.36 Li^+ reversibly exchanged (Figure 6a). Galvanostatic curves are similar to those obtained in a liquid medium (Figure 6b), indicating that the same electrochemical mechanism occurs with a good compatibility between the active material and the argyrodite. However, an inflection is observed at 0.12V, which is not present in galvanostatic measurements performed in a liquid medium. It may indicate a degradation of the argyrodite at very low potentials, which is one of the issues of this solid electrolyte [61,65]. The representation in Figure 6a allows us to highlight the overpotential or hysteresis, defined as the potential difference between the lithiation and delithiation curves. This difference is related to the kinetic limitations of the electrochemical reaction, in addition to the ohmic drop coming from the internal resistance of the half-cell [66]. It's worth noting that large hysteresis has a negative impact on battery performance, resulting in a reduction in specific energy density and energy efficiency.

Figure 6b illustrates the delithiation capacity and the coulombic efficiency as a function of the cycling number. Following the initial cycle, which exhibited a coulombic efficiency of 96%, the efficiency stabilized at 99 ± 1% over 17 cycles. This was accompanied by a reversible gravimetric capacity of 150 mAh g^{-1} followed by an irreversible drop in capacity. Such excellent reversibility is indicative of the fact that, even if argyrodite degradation is occurring at low potential, the corresponding reaction should be highly reversible.

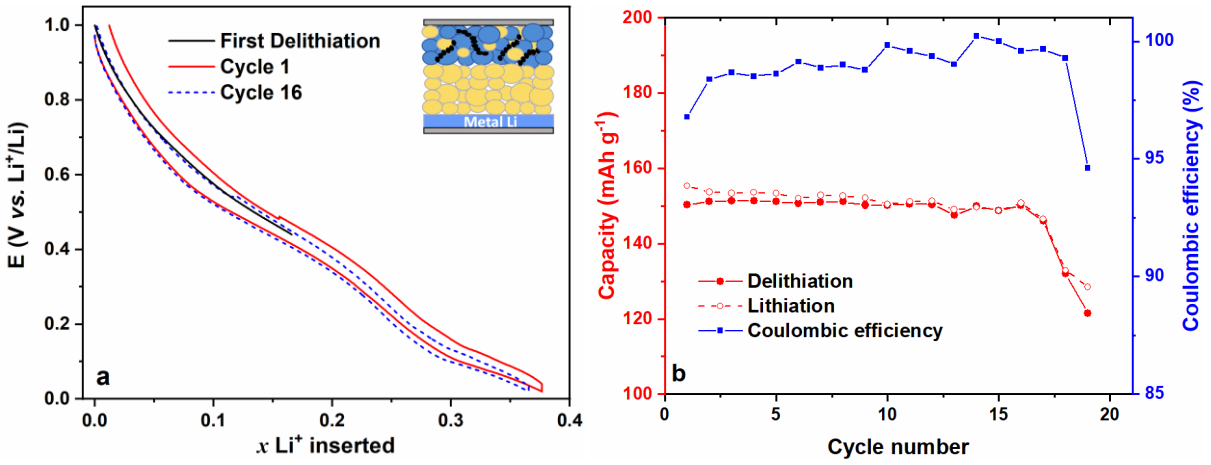

Figure 6: Long-term cycling of the $Li_{2.07}Ni_{0.62}N$ composite | Li_6PS_5Br | Li half-cell at 8 mA g^{-1} (C/25) within 0.02 – 1 V potential window: (a) Evolution of the potential profile and (b) lithiation / delithiation capacities and coulombic efficiency with the cycle number.

To gain insight into the mechanisms underlying battery failure, cyclic voltammetry was carried out using two distinct composite materials: (i) the nitride-argyrodite-carbon composite, which is employed in all-solid-state half cells (shown in blue in Figure 7a) and (ii) a composite comprising CVGF-argyrodite (shown in red in Figure 7b). These two experiments, with and without the nitride active material, are of interest in deciphering the nitride reversible electrochemical response from the argyrodite degradation at low potential. It appears that the nitride exhibits a broad reversible peak centered around 0.45 V, with a small shoulder around 0.7 V. These two contributions are absent in the nitride-free composite experiment as shown in Figure 7b. Such broad peaks are consistent with the solid solution behavior of the nitride electrode obtained in galvanostatic cycling because of a sloping potential profile. Below 0.2 V, two cathodic peaks at 0.07 and 0.10 V and three anodic peaks at 0.08, 0.12, and 0.18 V can be discernible in both experiments. Hence, this electrochemical signature at low potential is related to the argyrodite. Figure 7b and previous studies indicate that the degradation reactions of argyrodite are partially reversible and correspond to several changes in the oxidation state of phosphorus from P^{+V} in Li_6PS_5Br to P^{-III} in Li_3P [13,59]. Furthermore, the potential of the first cathodic peak explains the inflection at 0.12 V observed in the potential profile during galvanostatic cycling of the all-solid-state half-cell. Although this degradation appears to be electrochemically reversible, it may ultimately result in battery failure due to the accumulation of byproducts from argyrodite degradation at the interface with the nitride. To support this hypothesis, the lower voltage cut-off was elevated from 0.02 to 0.12 V for both configurations, including and excluding nitride active material (dot line, Figure7a-b). Thus, the low-voltage electrochemical signature is no longer observed, except for a weakly visible anodic peak at 0.18 V, which corresponds to the oxidation of degradation species of argyrodite formed within the 1 V – 0.12 V potential window. Consequently, this revised choice of the reduction cut-off potential is expected to limit the degradation of argyrodite.

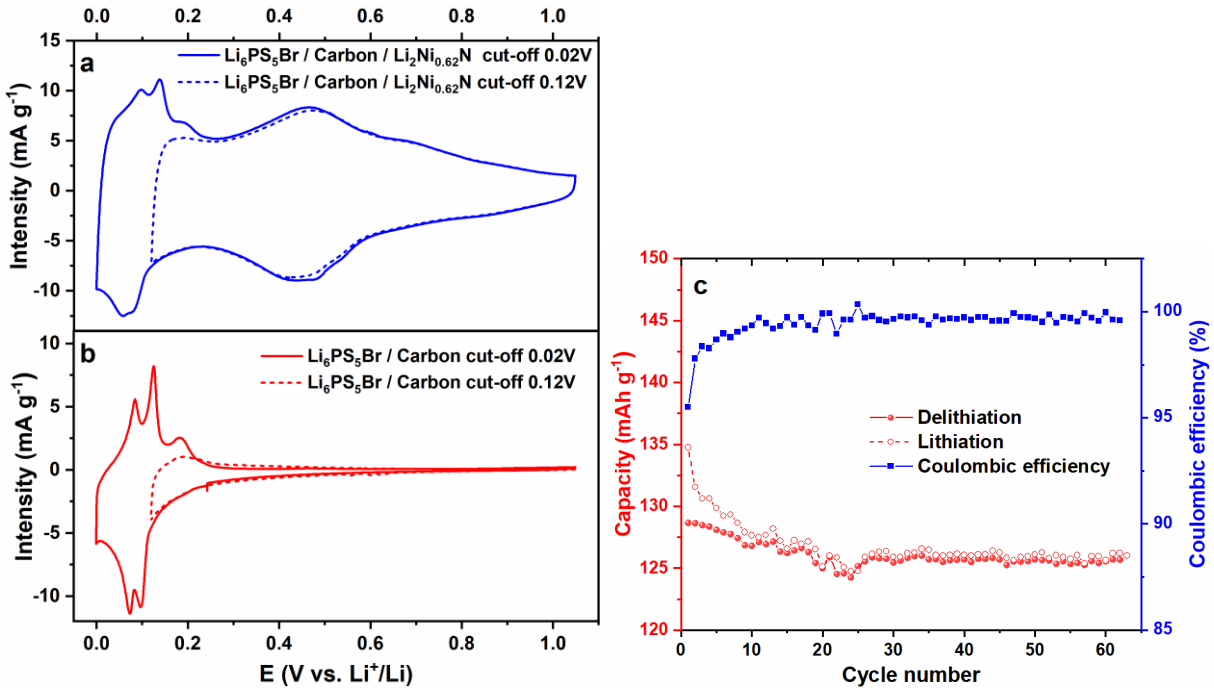

Figure 7: Cyclic voltammogram recorded at 10μV s^{-1} (cycle 2) within the potential range of 0.02 – 1 V (solid line) and 0.12 – 1 V (dotted line) for (a) $Li_{2.07}Ni_{0.62}N$ composite | Argyrodite | Li half-cell, (b) Argyrodite-CVGF | Argyrodite | Li half-cell. (c) Evolution of the lithiation / delithiation capacities and coulombic efficiencies as a function of cycle number for the $Li_{2.07}Ni_{0.62}N$ | Li_6PS_5Br | Li half-cell at 8 mA g^{-1} (C/25) within the potential range of 0.12-1V.

The cycle life of $Li_{2.07}Ni_{0.62}N$ was evaluated in all-solid-state half-cells within the 0.12 – 1 V voltage window at C/25 (Figure 7c). This cell exhibits an initial delithiation capacity of 128 mAh g^{-1} which remains stable after 62 cycles at 125 mAh g^{-1}, resulting in a capacity retention of 98% with a stable potential profile (see Figure S8). Throughout the cycling, a coulombic efficiency of 99.6 ± 0.2% was maintained. Compared to the low potential cut-off of 0.02 V, the reversible capacity is reduced by 20%; nevertheless, the battery's cycle life is significantly improved, maintaining satisfactory coulombic efficiency and capacity retention.

For the sake of comparison, galvanostatic cycling with chloride argyrodite as the solid electrolyte was carried out under the same conditions as its bromide counterpart (see Figure S9). It appears that the cycling performances were lower when chloride were used even with the new cut-off potential, which motivated the choice of bromide argyrodite as a solid electrolyte in this present work.

The rate performance of the active material was investigated by conducting lithiation/delithiation cycles at various C-rates (Figure 8a). The nitride demonstrates a reversible capacity ranging from 120 mAh g^{-1} at 5 mA g^{-1} to 96 mAh g^{-1} at 40 mA g^{-1}, corresponding to a capacity retention of 80%. The capacity at the lower rate is slightly less than the long-term cycling result shown in Figure 7c, which can be attributed to an error in the weight measurement of the active material. At C/5, the half-cell experienced a failure (Figure S10 shows the potential profile at C/5) during the last four delithiation steps, resulting in the absence of data in Figure 8a. Despite this issue, when the rate was reverted to 8 mA g^{-1}, the half-cell displayed a reversible capacity of 114 mAh g^{-1}, leading to a capacity retention of 95%. The sloping potential profile is preserved for the different C-rates with an overpotential ranging from 65 mV at 5 mA g^{-1} to 170 mV at 40 mA g^{-1} (Figure 8b), which is comparable to the overpotential obtained in a liquid medium of 113 mV at 40 mA g^{-1} [38,67]. The difference can be explained by the ohmic drop coming from the difference in ionic conductivity between the liquid and solid electrolyte.

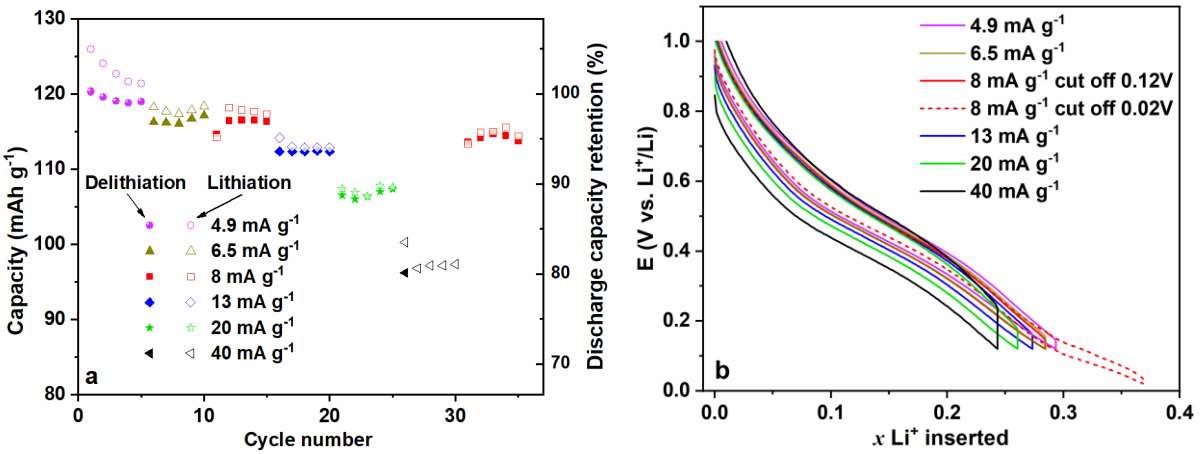

Figure 8: Rate performance of the $Li_{2.07}Ni_{0.62}N$ composite | Li_6PS_5Br | Li half-cell between 5 and 40 mA g^{-1} within 0.12-1V potential window. (a) Evolution of the lithiation / delithiation capacities, (b) Evolution of the potential profile at cycle 2 for each C-rate tested. For the sake of comparison, the preceding data employing a lithiation cut-off of 0.02 V has been included in the dotted line

Peukert's law, which relates battery capacity to the discharge rate (Eq. 3), was utilized to further investigate the effect of increasing current density on capacity:

$$C_P = I^k \cdot t \text{ (Eq. 3)}$$

Where C_p (Ah) is the capacity at 1 A discharge current, I (A) is the discharge current, t (h) is the discharge time, and k is the dimensionless Peukert coefficient. As shown in Figure S11, a Peukert coefficient of 1.1 was obtained, which is close to 1, indicating that the capacity is weakly impacted by the C-rate within the present range [68].

3.7 Study of the electrochemical mechanism by operando XRD

Operando XRD measurements were conducted throughout the first delithiation and the following two lithiation-delithiation cycles. The TOPAS package was employed to analyze the collected diffraction patterns. Figure 9 illustrates the comprehensive XRD pattern observed during the initial full cycle, following the first delithiation step, which is not shown here (see Figure S12 for the X-axis in 2θ). The diffraction peaks were successfully indexed as Li_6PS_5Br argyrodite (shown in green) and $Li_{2.07}Ni_{0.62}N$ nitride (purple color) within the composite of the working electrode. Throughout the entire cycle, the argyrodite peaks did not change in position or intensity, suggesting that the argyrodite structure and composition remained unchanged over these two cycles. Conversely, and as expected, the $Li_{2.07}Ni_{0.62}N$ peaks evolved with changes in their lithium content.

Starting from the delithiated nitride (red diffractogram pattern at the bottom of Figure 9), the (300) and $(2\bar{1}0)$ diffraction peaks shifted to lower Q values during the lithiation step, and the opposite process is observed during the delithiation step, resulting in an overlap of the red diffractogram pattern. This result demonstrates the full reversibility of the nitride structural

change during a galvanostatic cycle. The shift to lower Q values of the (300) and $(2\bar{1}0)$ diffraction peaks during lithiation indicates an increase of the lattice parameter *a,* which can be explained by lithium insertion into the vacancies of the 2*c* site, resulting in an expansion of the basal plane.

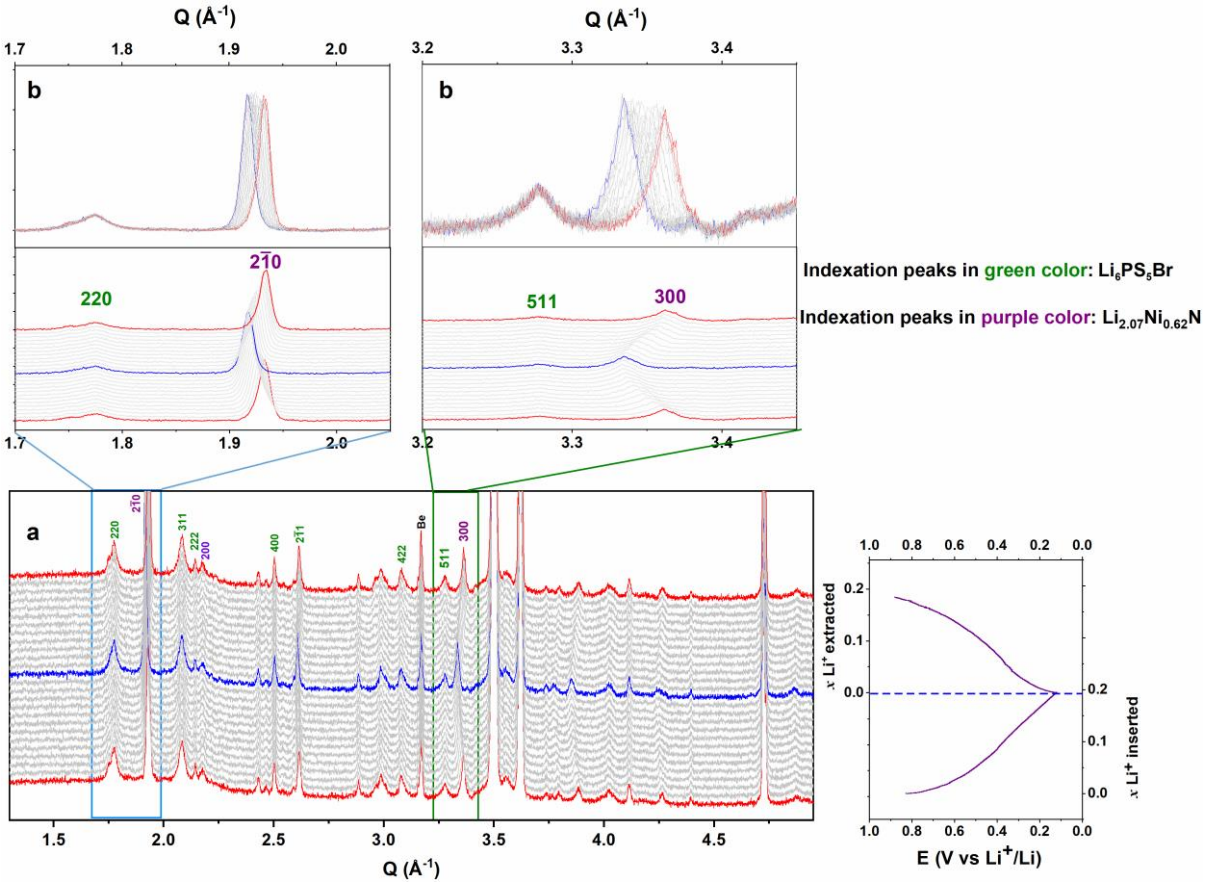

Figure 9: Operando XRD during galvanostatic cycling with (a) XRD patterns at different charge states, starting from delithiated nitride ($x_{inserted}$ = 0, pattern in red at the bottom), reaching lithiated nitride (x_{inserted} = 0.2, pattern in blue in the middle), and returning to delithiated nitride ($x_{\text{extracted}}$ = 0.2, pattern in red at the top). (b) Zoomed view of the displacement of the (300) and $(2\bar{1}0)$ diffraction peaks for $Li_{2.07}Ni_{0.62}N$, and the (220) and (511) diffraction peaks for the bromide argyrodite.

The lattice parameters *a* and *c,* obtained by Rietveld analysis, are plotted in Figure 10 as a function of the inserted lithium ion *x*. Upon lithiation with 0.2 Li^+ inserted, the in-plane parameter increases from 3.728 Å to 3.763 Å, representing a +0.9% variation, while a contraction in the interlayer distance is noted, decreasing the *c* parameter from 3.562 Å to 3.547 Å, representing a -0.4% variation. The opposite trend is observed during the extraction of lithium ions. As indicated above, the increase of t the *a* parameter during lithiation is a result of the lithium insertion into the 2*c* sites, while the *c* parameter decrease can be explained by a small distortion of the lattice, consisting of a shift of the Li_2N^- plane to accommodate the lithium insertion in the basal plane [37]. Ultimately, the overall volume expansion is confined to 1.4%

for 0.2 Li^+ insertions. Such a low expansion is beneficial for all-solid-state batteries, where the accommodation of volume expansion is a crucial issue.

The same trend was observed in a liquid medium for $Li_2Ni_{0.67}N$, demonstrating that the electrochemical storage mechanism is consistent in both all-solid-state and liquid configurations [37]. The lattice parameters and lattice volume variations were a 1.1% increase for parameter *a* and a 0.6% decrease for parameter *c*, resulting in a volume expansion of 2% for 0.5 Li^+ insertions during lithiation. This volume expansion is significantly lower than that of conversion-type anode materials such as Si or Sn, which form alloys with Li, resulting in high capacities but also substantial volume expansion of 410 and 260% respectively (see Table S1). In comparison to materials based on an insertion mechanism, $Li_2Ni_{0.67}N$ exhibits lower expansion than graphite (12%) or Li_7MnN_4 (7%). Although $Li_5Ti_4O_{12}$ (LTO) demonstrates the lowest volume expansion (1%), its relatively high working potential (1.6 V) limits its energy density compared to $Li_2Ni_{0.67}N$ (0.4 V).

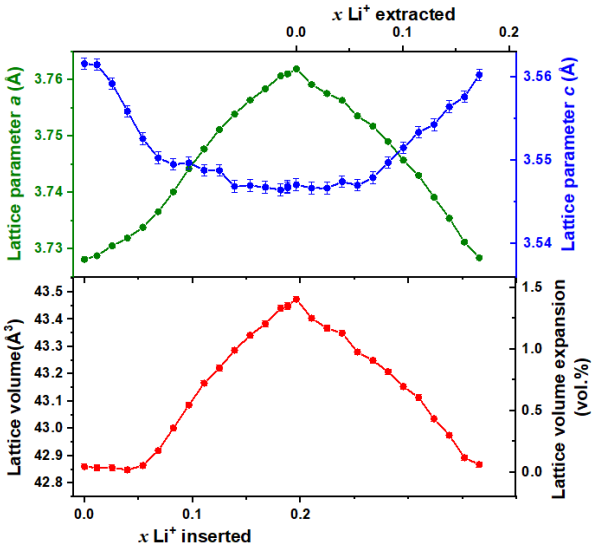

Figure 10: Evolution of the *a* and *c* lattice parameter along with the lattice volume for the P6/mmm Li_3N-type structure of $Li_{2.07}Ni_{0.62}N$, during the first cycle at 5.8 mA g^{-1} (after the first delithiation step, not presented).

3.8 Post-mortem XPS analysis

To further investigate the degradation process of argyrodite within the electrode composite, high-resolution XPS spectra of S2p and P2p were acquired before cycling and after battery failure, using a cut-off voltage of 0.12V (Figure 11). Due to the spin-orbit coupling, all spectra are deconvoluted with two specific components characteristic of $2p_{3/2}$ and $2p_{1/2}$ states in agreement with a peak area ratio of 0.5. In the pristine state, the S2p spectrum can be deconvoluted into two doublets, the main one (93 % in blue), at binding energies of 161.8 and 163 eV, is attributed to the PS_4^{3-} thiophosphate units in the 4*b*/16*e* site of the Li_6PS_5Br argyrodite. The second doublet (7 % in green), at binding energies of 160.4 and 161.5 eV, is

ascribed to the Li-S bonds originating from sulfur in the 4*a* and 4*c* sites, along with the Li_2S precursor [59,65,69]. The P 2p spectrum can be deconvoluted into two doublets, the first one (81% in blue), at binding energies of 132.2 and 133.1 eV (blue), is attributed to the PS_4^{3-} thiophosphate units, and the second one (19% in red), at binding energies of 132.8 and 133.7 eV, is ascribed to the P-S-P bound originating from remaining P_2S_5.[13,65,69]

Following battery failure, the S 2p chemical signature remains consistent, showing two doublets. However, the contribution from Li-S bonds at lower binding energy increases significantly, from 7% to 26%. This degradation involves a multi-step reaction that liberates elemental Li_2S through the reduction of $P^{(V)}$ to various reduced phosphorus species, such as $Li_4P^{(IV)}{}_2S_6$, $P^{(0)}$, $LiP^{(-I)}$ $Li_3P^{(-III)}$, within the 0–1.7 V potential window [65,70]. This is corroborated by the appearance of a broad new doublet in the P 2p spectrum at 130.3 and 131.2 eV (10%) assigned P reduced species, although this does not correspond to Li_3P, which is located in a lower energy band (127 eV) [13,59].

Given that the redox activity of phosphorus is partially reversible [70], a substantial accumulation of reduced phosphorus species is not observed. However, the increase in Li-S bonds in the S2p signal indicates that despite raising the cut-off potential from 0.02 to 0.12 V, argyrodite degradation is not entirely prevented. This degradation likely contributes to battery failure, although mechanical issues cannot be ruled out and require further investigation in future studies.

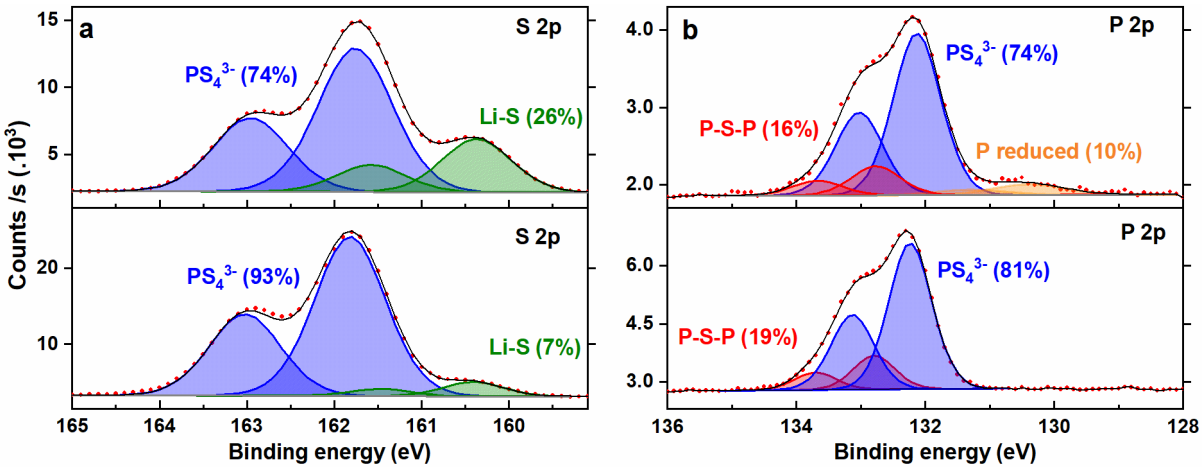

Figure 11: High-resolution XPS spectra of $Li_{2.07}Ni_{0.62}N$ composite prior to cycling (bottom) and after cycling until battery failure (top) of a) S2p and b) P2p signal. Experimental data in red dot, fitting data in black dash corresponding to the sum of the different contributions (filed curves)

Conclusion

In this study, we explored the coupling of bromide argyrodite Li_6PS_5Br as the solid electrolyte and lithium nitridonickelate $Li_{2.07}Ni_{0.62}N$ as the negative electrode material for all-solid-state lithium-ion batteries. The argyrodite was synthesized by mechanical milling. It

crystallized in the expected face-centered cubic (fcc) structure with antisite disorder, characterized by 52% of S^{2-} and 48% of Br^{-} occupying the 4*c* site. Consequently, the material demonstrated an ionic conductivity of 0.74 mS cm^{-1} at room temperature. The ball-milled argyrodite presented a critical current density for lithium dendrite formation of 0.25 mA cm^{-2}.

Lithium nitridonickelate exhibited a typical solid solution behavior with a sloping potential profile in the 0–1 V potential window in both liquid and all-solid-state configurations. However, cyclic voltammetry indicated a high electrochemical activity of the argyrodite in the 0–0.2 V potential window, leading to a short cycle life of the $Li_{2.1}Ni_{0.62}N$ /CVGF/Li_6PS_5Br electrode composite. Adjusting the potential window between 0.12 V and 1 V allowed cycling of the nitride active material between 5 and 40 mA g^{-1} with limited hysteresis and good capacity retention. Long-term cycling at 8 mA g^{-1} (C/25) demonstrated a stable capacity of 125 mAh g^{-1} over 62 cycles with a coulombic efficiency close to 100%. Operando XRD analysis confirmed that the electron storage mechanism is not different from the mechanism observed in a liquid medium. The present findings underscore the potential of lithium nitridonickelate materials as anode materials in ASSLIB configurations using argyrodite as the solid-state electrolyte. Future research will focus on optimizing the properties of bromide argyrodite through chemical substitutions to facilitate the development of full solid-state battery cells, using NMC as the positive electrode material.

Acknowledgment

The authors acknowledge the financial support of the MESRI (French Ministère de l'Enseignement supérieur, de la Recherche et de l'Innovation) through the "allocation doctorale" grant. The authors acknowledge Rémy Pires for the acquisition of SEM images and EDX chemical mapping.

Author contributions

Yaxin Qu: Conceptualization, Data curation, Formal analysis, Investigation, Methodology, Validation, Visualization, Writing – original draft, Writing – review & editing. **Mickael Mateos**: Conceptualization, Data curation, Formal analysis, Investigation, Methodology, Visualization, Writing – original draft, Writing – review & editing, Ressources Supervision, Project administration, Funding acquisition. **Junxian Zhang**: Conceptualization, Data curation, Formal analysis, Investigation, Methodology, Visualization, Writing – review & editing, Ressources Supervision, Project administration, Funding acquisition **Nicolas Emery**: Conceptualization, Data curation, Formal analysis, Investigation, Methodology, Visualization; Writing – review & editing. **Sandrine Zanna**: Investigation, Formal analysis, Methodology, Resources. **Dimitri Mercier**: Investigation, Formal analysis, Methodology, Resources. **Agustin Rios de Anda**: Investigation, Formal analysis, Methodology, Resources. **Fermin Cuevas**: Funding acquisition, Writing – review & editing. **Narimane Meziani**: Methodology.

References

[1] Y. Chen, Y. Kang, Y. Zhao, L. Wang, J. Liu, Y. Li, Z. Liang, X. He, X. Li, N. Tavajohi, B. Li, A review of lithium-ion battery safety concerns: The issues, strategies, and testing standards, Journal of Energy Chemistry 59 (2021) 83–99.
[2] H. Li, Practical Evaluation of Li-Ion Batteries, Joule 3 (2019) 911–914.
[3] J.B. Goodenough, Y. Kim, Challenges for Rechargeable Li Batteries, Chem. Mater. 22 (2010) 587–603.
[4] Issues and challenges facing rechargeable lithium batteries, MATERIALS FOR SUSTAINABLE ENERGY 414 (2010).
[5] A.L. Robinson, J. Janek, Solid-state batteries enter EV fray, MRS Bull. 39 (2014) 1046–1047.
[6] B. Scrosati, J. Garche, Lithium batteries: Status, prospects and future, Journal of Power Sources 195 (2010) 2419–2430.
[7] J. Janek, W.G. Zeier, A solid future for battery development, Nat Energy 1 (2016) 16141.
[8] X. Bai, Y. Duan, W. Zhuang, R. Yang, J. Wang, Research progress in Li-argyrodite-based solid-state electrolytes, J. Mater. Chem. A 8 (2020) 25663–25686.
[9] Y.-S. Choi, J.-C. Lee, Electronic and mechanistic origins of the superionic conductivity of sulfide-based solid electrolytes, Journal of Power Sources 415 (2019) 189–196.
[10] J. Lau, R.H. DeBlock, D.M. Butts, D.S. Ashby, C.S. Choi, B.S. Dunn, Sulfide Solid Electrolytes for Lithium Battery Applications, Adv. Energy Mater. 8 (2018) 1800933.
[11] J. Wu, S. Liu, F. Han, X. Yao, C. Wang, Lithium/Sulfide All-Solid-State Batteries using Sulfide Electrolytes, Adv. Mater. 33 (2021) 2000751.
[12] N. Kamaya, K. Homma, Y. Yamakawa, M. Hirayama, R. Kanno, M. Yonemura, T. Kamiyama, Y. Kato, S. Hama, K. Kawamoto, A. Mitsui, A lithium superionic conductor, Nature Mater 10 (2011) 682–686.
[13] D.H.S. Tan, E.A. Wu, H. Nguyen, Z. Chen, M.A.T. Marple, J.-M. Doux, X. Wang, H. Yang, A. Banerjee, Y.S. Meng, Elucidating Reversible Electrochemical Redox of Li_6PS_5Cl Solid Electrolyte, ACS Energy Letters (2019) 10.
[14] Y. Zhu, X. He, Y. Mo, Origin of Outstanding Stability in the Lithium Solid Electrolyte Materials: Insights from Thermodynamic Analyses Based on First-Principles Calculations, ACS Appl. Mater. Interfaces 7 (2015) 23685–23693.
[15] A. Orue Mendizabal, M. Cheddadi, A. Tron, A. Beutl, P. López-Aranguren, Understanding Interfaces at the Positive and Negative Electrodes on Sulfide-Based Solid-State Batteries, ACS Appl. Energy Mater. 6 (2023) 11030–11042.
[16] T. Chen, L. Zhang, Z. Zhang, P. Li, H. Wang, C. Yu, X. Yan, L. Wang, B. Xu, Argyrodite Solid Electrolyte with a Stable Interface and Superior Dendrite Suppression Capability Realized by ZnO Co-Doping, ACS Appl. Mater. Interfaces 11 (2019) 40808–40816.
[17] Z. Ning, G. Li, D.L.R. Melvin, Y. Chen, J. Bu, D. Spencer-Jolly, J. Liu, B. Hu, X. Gao, J. Perera, C. Gong, S.D. Pu, S. Zhang, B. Liu, G.O. Hartley, A.J. Bodey, R.I. Todd, P.S. Grant, D.E.J. Armstrong, T.J. Marrow, C.W. Monroe, P.G. Bruce, Dendrite initiation and propagation in lithium metal solid-state batteries, Nature 618 (2023) 287–293.
[18] C. Yang, K. Fu, Y. Zhang, E. Hitz, L. Hu, Protected Lithium-Metal Anodes in Batteries: From Liquid to Solid, Advanced Materials 29 (2017) 1701169.
[19] D. Wang, H. Shi, S. Wang, X. Wu, W. Jiang, S. Liang, Z. Xu, New insights into Li-argyrodite solid-state electrolytes based on doping strategies, Coordination Chemistry Reviews 508 (2024) 215776.
[20] B.D. Dandena, D.-S. Tsai, S.-H. Wu, W.-N. Su, B.J. Hwang, Roles of cation-doped Li-argyrodite electrolytes on the efficiency of all-solid-state-lithium batteries, Energy Storage Materials 69 (2024) 103305.
[21] L. Höltschi, C.N. Borca, T. Huthwelker, F. Marone, C.M. Schlepütz, V. Pelé, C. Jordy, C. Villevieille, M.E. Kazzi, P. Novák, Performance-limiting factors of graphite in sulfide-based all-solid-state lithium-ion batteries, Electrochimica Acta 389 (2021) 138735.

[22] X. Gao, X. Yang, M. Jiang, M. Zheng, Y. Zhao, R. Li, W. Ren, H. Huang, R. Sun, J. Wang, C.V. Singh, X. Sun, Fast Ion Transport in Li-Rich Alloy Anode for High-Energy-Density All Solid-State Lithium Metal Batteries, Advanced Functional Materials 33 (2023) 2209715.
[23] R. Miyazaki, T. Hihara, Charge-discharge performances of Sn powder as a high capacity anode for all-solid-state lithium batteries, Journal of Power Sources 427 (2019) 15–20.
[24] Y. Zhou, W. Feng, Y. Xu, X. Liu, S. Wang, Z. Lv, X. Li, Z. Wang, Z. Yang, Development of Silicon-Based Anode for Lithium-Ion Batteries and Its Application in Solid-State Electrolytes, Eng. Sci. (2023).
[25] S. Yubuchi, W. Nakamura, T. Bibienne, S. Rousselot, L.W. Taylor, M. Pasquali, M. Dollé, A. Sakuda, A. Hayashi, M. Tatsumisago, All-solid-state cells with $Li_4Ti_5O_{12}$/carbon nanotube composite electrodes prepared by infiltration with argyrodite sulfide-based solid electrolytes *via* liquid-phase processing, Journal of Power Sources 417 (2019) 125–131.
[26] C.M. Julien, A. Mauger, Fabrication of $Li_4Ti_5O_{12}$ (LTO) as Anode Material for Li-Ion Batteries, Micromachines 15 (2024) 310.
[27] F. Tan, H. An, N. Li, J. Du, Z. Peng, A study on $Li_{0.33}La_{0.55}TiO_3$ solid electrolyte with high ionic conductivity and its application in flexible all-solid-state batteries, Nanoscale 13 (2021) 11518–11524.
[28] E. Panabière, N. Emery, S. Bach, J.-P. Pereira-Ramos, P. Willmann, Ball-milled Li_7MnN_4: An attractive negative electrode material for lithium-ion batteries, Electrochimica Acta 97 (2013) 393–397.
[29] D. Muller-Bouvet, N. Emery, N. Tassali, E. Panabière, S. Bach, O. Crosnier, T. Brousse, C. Cénac-Morthe, A. Michalowicz, J.P. Pereira-Ramos, Unravelling redox processes of Li_7MnN_4 upon electrochemical Li extraction–insertion using operando XAS, Phys. Chem. Chem. Phys. 19 (2017) 27204–27211.
[30] M. Nishijima, T. Kagohashi, M. Imanishi, Y. Takeda, O. Yamamoto, S. Kondo, Synthesis and electrochemical studies of a new anode material, $Li_{3-x}Co_xN$, Solid State Ionics 83 (1996) 107–111.
[31] T. Shodai, S. Okada, S. Tobishima, J. Yamaki, Study of Li3 − xMxN (M: Co, Ni or Cu) system for use as anode material in lithium rechargeable cells, Solid State Ionics 86–88 (1996) 785–789.
[32] J. Cabana, Z. Stoeva, J.J. Titman, D.H. Gregory, M.R. Palacín, Towards New Negative Electrode Materials for Li-Ion Batteries: Electrochemical Properties of LiNiN, Chem. Mater. 20 (2008) 1676–1678.
[33] J.B. Ducros, S. Bach, J.P. Pereira-Ramos, P. Willmann, Comparison of the electrochemical properties of metallic layered nitrides containing cobalt, nickel and copper in the 1V–0.02V potential range, Electrochemistry Communications 9 (2007) 2496–2500.
[34] A. Kızılaslan, H. Akbulut, Assembling All-Solid-State Lithium–Sulfur Batteries with Li_3N-Protected Anodes, ChemPlusChem 84 (2019) 183–189.
[35] T. Fernandes, T. Cavoué, P. Berger, C. Barreteau, J.-C. Crivello, N. Emery, Chemical Composition of Lithiated Nitrodonickelates $Li_{3-xy}Ni_xN$: Evidence of the Intermediate Valence of Nickel Ions from Ion Beam Analysis and Ab Initio Calculations, Inorg. Chem. 62 (2023) 16013–16020.
[36] L.B. McCusker, R.B. Von Dreele, D.E. Cox, D. Louër, P. Scardi, Rietveld refinement guidelines, J Appl Crystallogr 32 (1999) 36–50.
[37] T. Cavoué, N. Emery, N. Umirov, S. Bach, P. Berger, Z. Bakenov, C. Cénac-Morthe, J.-P. Pereira-Ramos, $Li_{2.0}Ni_{0.67}N$, a Promising Negative Electrode Material for Li-Ion Batteries with a Soft Structural Response, Inorg. Chem. 56 (2017) 13815–13821.
[38] Y. Zhou, N. Emery, S. Franger, O. Nguyen, J.P. Pereira-Ramos, R. Baddour-Hadjean, Kinetic insights into LixNi0.67N (1.67 ≤ x ≤ 2.17), a quasi “zero-strain” negative electrode material for Li-ion battery, Journal of Power Sources 542 (2022) 231778.
[39] J.B. Leriche, S. Hamelet, J. Shu, M. Morcrette, C. Masquelier, G. Ouvrard, M. Zerrouki, P. Soudan, S. Belin, E. Elkaïm, F. Baudelet, An Electrochemical Cell for Operando Study of Lithium Batteries Using Synchrotron Radiation, J. Electrochem. Soc. 157 (2010) A606.

[40] S. Boulineau, Synthèses et caractérisations de matériaux céramiques, vitreux et vitrocéramiques à base de soufre, utilisables comme électrolytes dans les Batteries « Tout-Solide » Thèse de Doctorat Spécialité Sciences des Matériaux, phdthesis, Université de Picardie Jules Verne, 2013. https://tel.archives-ouvertes.fr/tel-01356443 (accessed August 29, 2022).
[41] Z. Zhang, J. Zhang, H. Jia, L. Peng, T. An, J. Xie, Enhancing ionic conductivity of solid electrolyte by lithium substitution in halogenated Li-Argyrodite, Journal of Power Sources 450 (2020) 227601.
[42] R.P. Rao, S. Adams, Studies of lithium argyrodite solid electrolytes for all-solid-state batteries, Physica Status Solidi (a) 208 (2011) 1804–1807.
[43] S. Boulineau, M. Courty, J.-M. Tarascon, V. Viallet, Mechanochemical synthesis of Li-argyrodite Li_6PS_5X (X=Cl, Br, I) as sulfur-based solid electrolytes for all solid state batteries application, Solid State Ionics 221 (2012) 1–5.
[44] C. Yu, L. Van Eijck, S. Ganapathy, M. Wagemaker, Synthesis, structure and electrochemical performance of the argyrodite Li_6PS_5Cl solid electrolyte for Li-ion solid state batteries, Electrochimica Acta 215 (2016) 93–99.
[45] A.R. Stamminger, B. Ziebarth, M. Mrovec, T. Hammerschmidt, R. Drautz, Ionic Conductivity and Its Dependence on Structural Disorder in Halogenated Argyrodites Li_6PS_5X (X = Br, Cl, I), Chem. Mater. 31 (2019) 8673–8678.
[46] M.A. Kraft, S.P. Culver, M. Calderon, F. Böcher, T. Krauskopf, A. Senyshyn, C. Dietrich, A. Zevalkink, J. Janek, W.G. Zeier, Influence of Lattice Polarizability on the Ionic Conductivity in the Lithium Superionic Argyrodites Li_6PS_5X (X = Cl, Br, I), J. Am. Chem. Soc. 139 (2017) 10909–10918.
[47] A. Gautam, M. Ghidiu, A.-L. Hansen, S. Ohno, W.G. Zeier, Sn Substitution in the Lithium Superionic Argyrodite Li_6PCh_5I (Ch = S and Se), Inorg. Chem. 60 (2021) 18975–18980.
[48] K. Hogrefe, I. Hanghofer, H.M.R. Wilkening, With a Little Help from ^{31}P NMR: The Complete Picture on Localized and Long-Range Li^+ Diffusion in Li_6PS_5I, J. Phys. Chem. C 125 (2021) 22457–22463.
[49] L. Zhou, K.-H. Park, X. Sun, F. Lalère, T. Adermann, P. Hartmann, L.F. Nazar, Solvent-Engineered Design of Argyrodite Li_6PS_5X (X = Cl, Br, I) Solid Electrolytes with High Ionic Conductivity, ACS Energy Lett. 4 (2019) 265–270.
[50] N. Minafra, M.A. Kraft, T. Bernges, C. Li, R. Schlem, B.J. Morgan, W.G. Zeier, Local Charge Inhomogeneity and Lithium Distribution in the Superionic Argyrodites Li_6PS_5X (X = Cl, Br, I), Inorg. Chem. 59 (2020) 11009–11019.
[51] B. Morgan, Mechanistic Origin of Superionic Lithium Diffusion in Anion-Disordered Li_6PS_5X Argyrodites, Chem. Mater. 33 (2021) 2004–2018.
[52] I. Hanghofer, M. Brinek, S.L. Eisbacher, B. Bitschnau, M. Volck, V. Hennige, I. Hanzu, D. Rettenwander, H.M.R. Wilkening, Substitutional disorder: structure and ion dynamics of the argyrodites Li_6PS_5Cl, Li_6PS_5Br and Li_6PS_5I, Phys. Chem. Chem. Phys. 21 (2019) 8489–8507.
[53] C. Yu, S. Ganapathy, E.R.H. van Eck, L. van Eijck, S. Basak, Y. Liu, L. Zhang, H.W. Zandbergen, M. Wagemaker, Revealing the relation between the structure, Li-ion conductivity and solid-state battery performance of the argyrodite Li_6PS_5Br solid electrolyte, J. Mater. Chem. A 5 (2017) 21178–21188.
[54] Z. Zhang, L. Zhang, Y. Liu, C. Yu, X. Yan, B. Xu, L. Wang, Synthesis and characterization of argyrodite solid electrolytes for all-solid-state Li-ion batteries, Journal of Alloys and Compounds 747 (2018) 227–235.
[55] C. Yu, Y. Li, W. Li, K.R. Adair, F. Zhao, M. Willans, J. Liang, Y. Zhao, C. Wang, S. Deng, R. Li, H. Huang, S. Lu, T.-K. Sham, Y. Huang, X. Sun, Enabling ultrafast ionic conductivity in Br-based lithium argyrodite electrolytes for solid-state batteries with different anodes, Energy Storage Materials 30 (2020) 238–249.
[56] A. Gautam, H. Al-Kutubi, T. Famprikis, S. Ganapathy, M. Wagemaker, Exploring the Relationship Between Halide Substitution, Structural Disorder, and Lithium Distribution in Lithium Argyrodites ($Li_{6-x}PS_{5-x}Br_{1+x}$), Chem. Mater. 35 (2023) 8081–8091.

[57] A. Gautam, M. Sadowski, N. Prinz, H. Eickhoff, N. Minafra, M. Ghidiu, S.P. Culver, K. Albe, T.F. Fässler, M. Zobel, W.G. Zeier, Rapid Crystallization and Kinetic Freezing of Site-Disorder in the Lithium Superionic Argyrodite Li_6PS_5Br, Chem. Mater. 31 (2019) 10178–10185.
[58] J. Auvergniot, A. Cassel, J.-B. Ledeuil, V. Viallet, V. Seznec, R. Dedryvère, Interface Stability of Argyrodite Li_6PS_5Cl toward $LiCoO_2$, $LiNi_{1/3}Co_{1/3}Mn_{1/3}O_2$, and $LiMn_2O_4$ in Bulk All-Solid-State Batteries, Chem. Mater. 29 (2017) 3883–3890.
[59] S. Wenzel, S.J. Sedlmaier, C. Dietrich, W.G. Zeier, J. Janek, Interfacial reactivity and interphase growth of argyrodite solid electrolytes at lithium metal electrodes, Solid State Ionics 318 (2018) 102–112.
[60] Z. Zhang, L. Zhang, X. Yan, H. Wang, Y. Liu, C. Yu, X. Cao, L. Eijck, B. Wen, All-in-one improvement toward Li_6PS_5Br-Based solid electrolytes triggered by compositional tune | Elsevier Enhanced Reader, Journal of Power Sources 410-411 (2019) 162-170.
[61] A. Orue Mendizabal, M. Cheddadi, A. Tron, A. Beutl, P. López-Aranguren, Understanding Interfaces at the Positive and Negative Electrodes on Sulfide-Based Solid-State Batteries, ACS Appl. Energy Mater. 6 (2023) 11030–11042.
[62] T. Cavoué, N. Emery, N. Umirov, S. Bach, P. Berger, Z. Bakenov, C. Cénac-Morthe, J.-P. Pereira-Ramos, $Li_{2.0}Ni_{0.67}N$, a Promising Negative Electrode Material for Li-Ion Batteries with a Soft Structural Response, Inorg. Chem. 56 (2017) 13815–13821.
[63] J.B. Ducros, S. Bach, J.P. Pereira-Ramos, P. Willmann, Optimization of cycling properties of the layered lithium cobalt nitride $Li_{2.2}Co_{0.4}N$ as negative electrode material for Li-ion batteries, Electrochimica Acta 167 (2015) 20–24.
[64] J.C. Bachman, S. Muy, A. Grimaud, H.-H. Chang, N. Pour, S.F. Lux, O. Paschos, F. Maglia, S. Lupart, P. Lamp, L. Giordano, Y. Shao-Horn, Inorganic Solid-State Electrolytes for Lithium Batteries: Mechanisms and Properties Governing Ion Conduction, Chem. Rev. 116 (2016) 140–162.
[65] K. Ando, T. Matsuda, T. Miwa, M. Kawai, D. Imamura, Degradation mechanism of all-solid-state lithium-ion batteries with argyrodite $Li_{7-x}PS_{6-x}Cl_x$ sulfide through high-temperature cycling test, Battery Energy 2 (2023) 20220052.
[66] A. Van der Ven, K.A. See, L. Pilon, Hysteresis in electrochemical systems, Battery Energy 1 (2022) 20210017.
[67] Y. Zhou, Structure and electrochemistry of lithiated transition metal (Mn, Fe, Ni) nitrides as materials for negative electrode of lithium ion battery, These de doctorat, Paris 12, 2022. https://theses.fr/2022PA120065 (accessed July 26, 2024).
[68] C. Nebl, F. Steger, H.-G. Schweiger, Discharge Capacity of Energy Storages as a Function of the Discharge Current–Expanding Peukert's equation, International Journal of Electrochemical Science 12 (2017) 4940–4957.
[69] J. Auvergniot, A. Cassel, D. Foix, V. Viallet, V. Seznec, R. Dedryvère, Redox activity of argyrodite Li_6PS_5Cl electrolyte in all-solid-state Li-ion battery: An XPS study, Solid State Ionics 300 (2017) 78–85.
[70] T.K. Schwietert, V.A. Arszelewska, C. Wang, C. Yu, A. Vasileiadis, N.J.J. de Klerk, J. Hageman, T. Hupfer, I. Kerkamm, Y. Xu, E. van der Maas, E.M. Kelder, S. Ganapathy, M. Wagemaker, Clarifying the relationship between redox activity and electrochemical stability in solid electrolytes, Nat. Mater. 19 (2020) 428–435.